Carrier-Based Model Predictive Pulse Pattern Control

Tobias Geyer, *Senior Member, IEEE*, and Vedrana Spudić, *Member, IEEE*

***Abstract*—Model predictive pulse pattern control (MP^{3}C) achieves fast closed-loop control of pre-computed optimized pulse patterns (OPPs) by manipulating their switching instants. Such OPPs, however, can only be computed and stored for low pulse numbers. To extend the MP^{3}C methodology to high pulse numbers, carrier-based pulse width modulation switching patterns are generated online and fed to the MP^{3}C switching time modification mechanism that controls the flux vector along a circular trajectory. In a variable speed drive, this extension makes MP^{3}C applicable to all operating points, ranging from standstill operation to field weakening at high speeds.**

I. Introduction

Optimized pulse patterns (OPPs) are a specific pulse width modulation (PWM) method that are typically computed off-line [1]. Unlike carrier-based PWM (CB-PWM) or space vector modulation (SVM), OPPs abandon the notion of the fixed modulation interval with one switching transition per modulation half-interval and phase [2]. The removal of this restriction facilitates the computation of optimal switching angles that minimize the harmonic current distortions for a given switching frequency [3].

To simplify the OPP computation, quarter- and half-wave symmetry and a 120° phase shift between the three phases is typically assumed [4]. With this, d switching angles and d switch positions need to be derived for one phase over a quarter of a fundamental period. For three-level OPPs and neutral point clamped (NPC) converters, the natural number d is equal to the pulse number. The latter states the switching frequency of a semiconductor device as $f_{\text{sw}} = df_1$, where f_1 is the frequency of the fundamental component.

The use of OPPs with high pulse numbers (e.g. $d \geq 20$) faces the following practical limitations: (i) the offline computation of such OPPs is demanding and time consuming, (ii) these OPPs require a significant amount of storage capacity in the controller memory, and (iii) the incentive to use OPPs diminishes, as the harmonic benefit of OPPs over established modulation methods is significantly reduced at high pulse numbers.

The need to operate at high pulse numbers arises naturally when operating at low fundamental frequencies; in drive applications, low fundamental frequencies correspond to low-speed operation. In power converters, the semiconductor losses and the adopted cooling technology usually impose the upper bound $f_{\text{sw,max}}$ on the switching frequency. When the fundamental frequency f_1 varies, the pulse number needs to be adjusted according to $d = \text{floor}(f_{\text{sw,max}}/f_1)$. Thus, as the drive speed is lowered and the fundamental frequency reduces, the required pulse number increases, theoretically towards infinity at zero fundamental frequency.

OPP-based control methods typically solve this issue by switching at high pulse numbers to another control loop that is based on CB-PWM or SVM modulation principles [5]. Field-oriented control with two orthogonal PI control loops is typically used for machine-side inverters [6]. However, the use of two control loops carries three disadvantages: (i) the switching between the two control loops introduces a disturbance and often glitches in the switching pattern, (ii) the appropriate initialization of the integrators in the PI controllers is challenging and can cause undesired transient behaviour if not done properly, and (iii) the controller implementation has an increased size and complexity.

To address these issues—and without switching to another control loop—the operation of model predictive pulse pattern control (MP^{3}C) [7] can be extended to the low fundamental frequency (i.e., high pulse number) regime. At each sampling instant, a CB-PWM switching pattern is generated online over several modulation cycles that cover at least the prediction horizon of MP^{3}C. This switching pattern is fed to the MP^{3}C switching time modification mechanism that controls the flux vector along a circular trajectory. We refer to this control method as carrier-based MP^{3}C.

Carrier-based MP^{3}C extends the OPP-based MP^{3}C control methodology to all operating points of a drive system, from operation at zero fundamental frequency to high-speed operation with pulse number one. The switching between OPPs and CB-PWM-generated switching patterns is handled seamlessly by MP^{3}C, similar to a transition between two OPPs with different pulse numbers. In particular, switching between two different control loops and the initialization of controller integrator states is avoided.

II. Preliminaries

To illustrate carrier-based MP^{3}C, we will focus on a three-phase three-level neutral point clamped (NPC) voltage source inverter connected to a medium-voltage induction machine (IM). The inverter has the total (instantaneous) dc-link voltage $v_{\text{dc}} = v_{\text{dc,up}} + v_{\text{dc,lo}}$, where $v_{\text{dc,up}}$ and $v_{\text{dc,lo}}$ denote the voltages over the upper and lower dc-link capacitors, respectively. The potential $v_n = \frac{1}{2}(v_{\text{dc,lo}} - v_{\text{dc,up}})$ of the neutral point (NP) between the two dc-link capacitors floats.

We introduce a per unit system and adopt normalized quantities. The base quantities are the peak value of the

The authors are with ABB Corporate Research, Baden-Dättwil, Switzerland; e-mail: t.geyer@ieee.org, vedrana.spudic@ch.abb.com

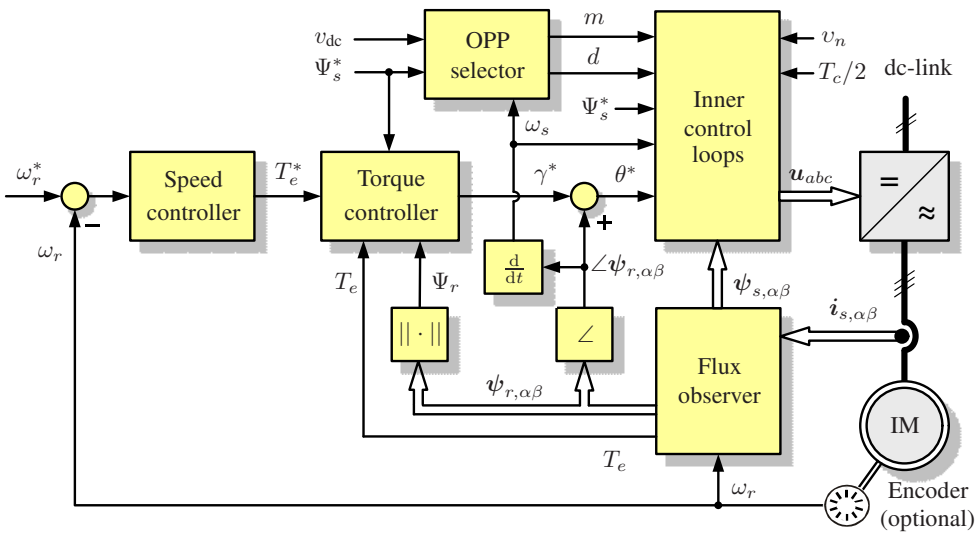

Fig. 1: Outer control loops of MP^{3}C

machine's rated phase voltage, the peak value of the rated machine current, and the rated fundamental frequency.

All variables $\boldsymbol{\xi}_{abc} = [\xi_a\ \xi_b\ \xi_c]^T$ in the three-phase system (abc) are transformed to $\boldsymbol{\xi}_{\alpha\beta 0} = [\xi_\alpha\ \xi_\beta\ \xi_0]^T$ in the stationary orthogonal $\alpha\beta 0$ coordinate system through the Clarke transformation $\boldsymbol{\xi}_{\alpha\beta 0} = \boldsymbol{K}\,\boldsymbol{\xi}_{abc}$. The inverse Clarke transformation is given by $\boldsymbol{\xi}_{abc} = \boldsymbol{K}^{-1}\boldsymbol{\xi}_{\alpha\beta 0}$. Because we often require only the differential-mode components, we also define the reduced Clarke transformation $\boldsymbol{\xi}_{\alpha\beta} = \tilde{\boldsymbol{K}}\boldsymbol{\xi}_{abc}$ and the reduced inverse Clarke transformation $\boldsymbol{\xi}_{abc} = \tilde{\boldsymbol{K}}^{-1}\boldsymbol{\xi}_{\alpha\beta}$. $\tilde{\boldsymbol{K}}$ holds the first two rows of $\boldsymbol{K}$, and $\tilde{\boldsymbol{K}}^{-1}$ holds the first two columns of $\boldsymbol{K}^{-1}$.

III. Outer Control Loops

The block diagram of the outer control loops of MP^{3}C is shown in Fig. 1. The different control blocks are briefly described hereafter:

- Based on the measured stator current vector $\boldsymbol{i}_{s,\alpha\beta}$ and the stator voltage $\boldsymbol{v}_{s,\alpha\beta}$, the flux observer estimates the stator and the rotor flux vectors $\boldsymbol{\psi}_{s,\alpha\beta}$ and $\boldsymbol{\psi}_{r,\alpha\beta}$, respectively. The estimate of the electromagnetic torque T_e follows directly.
- The speed controller regulates the (electrical) angular speed ω_r of the rotor along its reference ω_r^* by manipulating the setpoint of the electromagnetic torque T_e^*.
- The torque controller manipulates the desired load angle γ^*, i.e. the desired angle between the stator and the rotor flux vectors. The torque controller requires the reference of the stator flux magnitude Ψ_s^* and the actual magnitude of the rotor flux vector $\Psi_r = ||\boldsymbol{\psi}_{r,\alpha\beta}||$.
- The OPP selector sets the modulation index based on the expression $m = \omega_s \Psi_s^*\, 2/v_{\text{dc}}$. In here, ω_s is the angular stator frequency at which the flux vectors rotate during steady-state operation, and Ψ_s^* denotes the reference magnitude of the stator flux vector. The pulse number is chosen according to $d = \text{floor}(f_{\text{sw,max}}/f_1)$.

For more details on the principle of MP^{3}C and its different controller entities, the interested reader is referred to [7] and particularly to [4]. Techniques to control the NP potential in the framework of MP^{3}C are discussed in [8]. The addition of switching transitions to achieve fast current and torque transients is described in [9].

IV. Inner Control Loops of Carrier-Based MP^{3}C

The inner control loops of OPP-based MP^{3}C are explained in detail in [4], [7]. OPP-based MP^{3}C is restricted to low pulse numbers, say below 20. For higher pulse numbers, we replace the offline computed OPPs with online generated switching patterns. These patterns are then used in the MP^{3}C mechanism that modifies the switching instants and thus controls the stator flux of the machine.

The block diagram of the proposed inner control loops of carrier-based MP^{3}C is shown in Fig. 2. It consists of the following control blocks:

1) Flux reference and modulating signal: Computation of the flux reference $\boldsymbol{\psi}_{s,\alpha\beta}^*$ and computation of a suitable differential-mode modulating signal $\boldsymbol{u}_{abc}^*$.
2) Common mode: Addition of a common-mode component u_0^* to the modulating signal.
3) Pattern generation: Online generation of an appropriate CB-PWM switching pattern over multiple modulation cycles.
4) Pattern controller: Use of the known MP^{3}C pattern modification technique from [7] that modifies the switching instants over a prediction horizon.

Hereafter, the computational steps of the proposed carrier-based MP^{3}C approach are described.

A. Flux Reference and Differential-Mode Modulating Signal

Carrier-based MP^{3}C is intended for use at high pulse numbers, i.e. at high ratios between the switching frequency

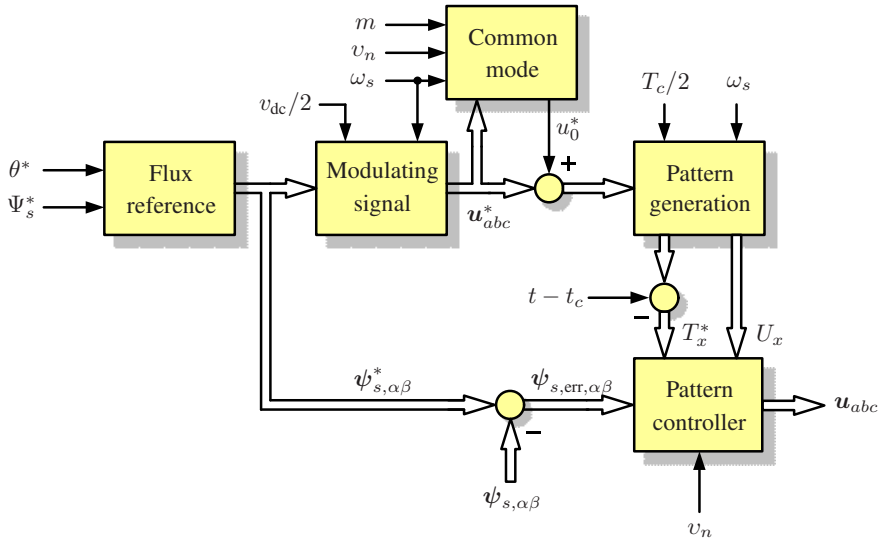

Fig. 2: Inner control loops of carrier-based MP^{3}C

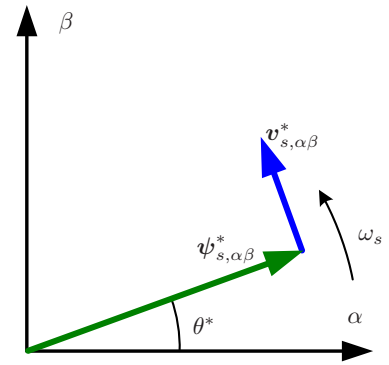

Fig. 3: Stator flux reference vector $\boldsymbol{\psi}_{s,\alpha\beta}^*$ and the corresponding differential-mode stator voltage reference vector $\boldsymbol{v}_{s,\alpha\beta}^*$

and the fundamental frequency. This allows us to approximate the stator flux trajectory by a circle, thus simplifying the implementation of the controller. Given the stator flux reference in terms of its angle $\theta^* = \angle\boldsymbol{\psi}_{r,\alpha\beta} + \gamma^*$ and magnitude Ψ_s^*, the stator flux reference vector in stationary orthogonal coordinates is

$$\boldsymbol{\psi}_{s,\alpha\beta}^* = \Psi_s^* \begin{bmatrix} \cos(\theta^*) \\ \sin(\theta^*) \end{bmatrix} . \tag{1}$$

During steady-state operation, the reference angle is given by $\theta^* = \omega_s t$, where ω_s is the angular stator frequency. Therefore, as shown in Fig. 3, the stator flux vector rotates with ω_s.

To simplify the derivation of the stator voltage reference, we neglect the stator resistance[1]. The stator voltage reference

$$\boldsymbol{v}_{s,\alpha\beta}^* = \frac{\mathrm{d}}{\mathrm{d}t}\boldsymbol{\psi}_{s,\alpha\beta}^* \tag{2}$$

is then the derivative of the stator flux reference. Inserting (1) into (2) leads to the expression

$$\boldsymbol{v}_{s,\alpha\beta}^* = \Psi_s^* \, \omega_s \begin{bmatrix} -\sin(\theta^*) \\ \cos(\theta^*) \end{bmatrix} = \omega_s \begin{bmatrix} 0 & -1 \\ 1 & 0 \end{bmatrix} \boldsymbol{\psi}_{s,\alpha\beta}^* , \tag{3}$$

where we used the fact that the time derivative of the reference angle θ^* is the angular stator frequency ω_s. The stator voltage reference is thus equal to the stator flux reference rotated forward by 90 degrees and scaled by the angular stator frequency. This is shown in Fig. 3.

The three-phase (differential-mode) modulating signal is

$$\boldsymbol{u}_{abc}^* = \frac{2}{v_{\mathrm{dc}}} \tilde{\boldsymbol{K}}^{-1} \boldsymbol{v}_{s,\alpha\beta}^* . \tag{4}$$

[1]The resulting error in the voltage vector is compensated by the pattern controller, see Sect. IV-D. The pattern controller regulates the stator flux vector along its circular trajectory and thus compensates for the unmodeled resistive voltage drop over the stator resistance. Specifically, by modifying the switching instants of the switching pattern, the applied voltage vector is modified accordingly.

The stator flux reference vector is computed in the block "flux reference" in Fig. 2 using (1). The block "modulating signal" is based on (3) and (4).

B. Common-Mode Voltage Injection

The block "common mode" in Fig. 2 adds the common-mode component u_0^* to the three-phase modulating signal. At very low speed, this is done to avoid overly narrow switching pulses and an uneven distribution of the semiconductor losses between the upper and the lower inverter half. In normal speed operation, the current distortions can be reduced by injecting an appropriate common-mode component.

1) Low-Speed Operation: When operating at very low speed and correspondingly very low modulation indices, such as $m \in [0,\ 0.02]$, the modulating signal has a very small amplitude. As a result, the switch positions are mostly zero with very short positive (negative) pulses during the positive (negative) half-wave of the modulating signal. These pulses must meet a certain minimum width in time, the so called on-time. In high-power converters, the minimum on-time can be as long as $t_{\mathrm{min}} = 50\,\mu\mathrm{s}$. Pulses of width between 0 and t_{min} must either be extended to t_{min} or removed. As a result, switching might be avoided altogether when operating at very low modulation indices, jeopardizing closed-loop control of the machine currents and stator flux.

To avoid the dropping of pulses, a suitable common-mode component u_0^* can be injected. For instance, when operating at a small (non-negative) modulation index, the positive common-mode signal

$$u_0^* = m + \frac{t_{\mathrm{min}}}{T_c} \tag{5}$$

shifts the modulating signal of all three phases into the positive half and ensures that the minimum pulse width of t_{min} is met. The offset t_{min}/T_c in (5) directly results from the rule of proportions applied to the carrier interval T_c and the modulating signals.

The second issue, the uneven distribution of the semiconductor losses, is caused by the low fundamental frequency. For sinusoidal CB-PWM, during half the fundamental period, only the switches in the upper (or the lower) inverter half are used. To mitigate this issue, the injection of a sufficiently large common-mode signal as in (5) can be used to periodically shift the semiconductor losses from the upper to the lower inverter half, and vice versa. This approach distributes the losses more evenly, avoiding the need to derate the inverter or to lower the switching frequency.

As a side effect, an offset in the modulating signal adds a bias to the NP current, thus increasing or decreasing the NP potential v_n. By flipping the sign of the common-mode term, the sign of the derivative of the NP potential can be reversed. This relationship is exploited by the hysteresis controller

$$\sigma_0(k) = \begin{cases} -\sigma_0(k-1) & \text{if } |v_n(k)| \geq v_{n,\max} \\ \sigma_0(k-1) & \text{otherwise} \end{cases} \tag{6}$$

that keeps the NP potential v_n within $-v_{n,\max}$ and $v_{n,\max}$. The to-be-injected common-mode component is then $u_0^*(k) = \hat{u}_0\,\sigma_0(k)$, where the non-negative scalar $\hat{u}_0$ is a design parameter. For $m \in [0,\ 0.02]$, for example, $\hat{u}_0 \geq m + \frac{t_{\min}}{T_c}$ should be used in accordance with (5).

This control scheme, which balances the NP potential at low-speed operation while ensuring switching pulses of a minimum width, is part of the block "common mode" in Fig. 2.

2) Normal-Speed Operation: At higher modulation indices, say $m > 0.02$, the issue of overly short switching pulses is not present. Instead, it is expedient to inject an appropriate common-mode component to the modulating signal to reduce the current distortions. Particularly SVM tends to reduce the current distortions. Switching patterns that mimic SVM are achieved by injecting the term

$$u_0^* = \bar{u}_0^* + \frac{1}{2} - \frac{1}{2}(\min(\bar{\boldsymbol{u}}_{abc}^*) + \max(\bar{\boldsymbol{u}}_{abc}^*))\,, \tag{7}$$

which is based on the scalar and three-phase terms

$$\bar{u}_0^* = -\frac{1}{2}(\min(\boldsymbol{u}_{abc}^*) + \max(\boldsymbol{u}_{abc}^*)) \tag{8}$$

$$\bar{\boldsymbol{u}}_{abc}^* = (\boldsymbol{u}_{abc}^* + \bar{u}_0^* + 1) \bmod 1\,. \tag{9}$$

The expression $\xi \bmod 1$ in (9) is defined as the remainder of the Euclidean division of ξ by one. The result is bounded between zero and one.

Adding (7) to the modulating signal makes CB-PWM with phase disposition equivalent to SVM, in the sense that both methods yield the same switching pattern when supplied with the same (differential-mode) modulating signal. This equivalence was shown in [10]. The addition of (7) to CB-PWM facilitates a simple and versatile implementation of SVM. It also increases the linear modulation region from $m = 1$ to 1.155.

Control of the NP potential can be achieved by manipulating the common-mode component of the modulating signal. A positive common-mode component, for example, shifts the phase voltages to the upper inverter half. Depending on the sign of the phase current (or the direction of the power flow), this shift adds a positive or negative bias to the average current drawn from the NP [11], which, in turn, modifies the NP potential. Exploiting this principle, a dedicated NP controller can be designed, similar to the one proposed in [12].

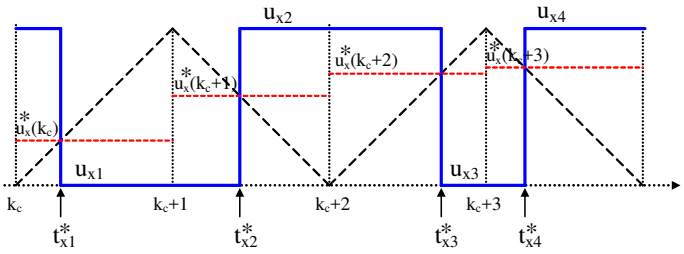

Fig. 4: Single-phase pattern generation in phase x over $K = 4$ carrier half-intervals

Polarity of the modulating signal u_x^*	Carrier slope	Switching instant t_x	Switching transition for u_x
≥ 0	Falling	$(1 - u_x^*)\frac{T_c}{2}$	$0 \rightarrow 1$
≥ 0	Rising	$u_x^* \frac{T_c}{2}$	$1 \rightarrow 0$
< 0	Falling	$-u_x^* \frac{T_c}{2}$	$-1 \rightarrow 0$
< 0	Rising	$(1 + u_x^*)\frac{T_c}{2}$	$0 \rightarrow -1$

TABLE I: Nominal switching instant and switching transition for phase x, with $x \in \{a, b, c\}$, when generating the switching pattern of asymmetric regularly sampled CB-PWM

C. Online Generation of CB-PWM Switching Patterns

Consider CB-PWM with the carrier frequency f_c and the carrier interval $T_c = 1/f_c$. We assume carriers with phase disposition and asymmetric regular sampling, i.e., sampling of the modulating signal at the upper and lower peaks of the triangular carrier signal. We denote these sampling instants by $t_c = 0.5T_c k_c$, where $k_c \in \mathbb{N}$.

The block "pattern generation" in Fig. 2 generates in each phase $x \in \{a, b, c\}$ a switching table that consists of the pair of vectors T_x^* and U_x. The former captures the nominal switching instants, whereas the latter contains the single-phase switch positions of phase x. The switching tables are updated at the discrete time steps k_c, as indicated in Fig. 4. Each table spans a prediction horizon of K carrier half-intervals from $0.5T_c k_c$ to $0.5T_c(k_c + K - 1)$. We introduce the time step ℓ_c to denote these half-intervals, where $\ell_c \in \{0, 1, \ldots, K-1\}$.

To compute the switching tables at time step k_c, the sampled modulating signal $\boldsymbol{u}_{abc}^*(k_c)$ is translated into the $\alpha\beta 0$ coordinate system through the Clarke transformation, and then rotated forward ℓ_c times assuming a constant angular frequency ω_s. This allows us to predict future samples of the modulating signal at time steps $k_c + \ell_c$.

We introduce the integer variable $\sigma_c(k_c+\ell_c) = (-1)^{(k_c+\ell_c)}$, with $\sigma_c \in \{-1, 1\}$, to indicate the sign of the carrier slope at time step $k_c + \ell_c$. The nominal switching instants relative to the time instant t_c are obtained through linear mappings of the modulating signal. These mappings depend on the polarity of the modulating signal and the carrier slope, leading to four different cases, as summarized in Table I.

The (ℓ_c+1)th switching transition in phase x occurs at the nominal time instant

$$t^*_{x(\ell_c+1)} = 0.5T_c\ell_c + \frac{T_c}{2}. \tag{10}$$

$$\begin{cases} \big(1-u^*_x(k_c+\ell_c)\big) & \text{if } u^*_x(k_c+\ell_c)\geq 0 \text{ and } \sigma_c(k_c+\ell_c)=-1 \\ u^*_x(k_c+\ell_c) & \text{if } u^*_x(k_c+\ell_c)\geq 0 \text{ and } \sigma_c(k_c+\ell_c)=1 \\ (-1)u^*_x(k_c+\ell_c) & \text{if } u^*_x(k_c+\ell_c)< 0 \text{ and } \sigma_c(k_c+\ell_c)=-1 \\ \big(1+u^*_x(k_c+\ell_c)\big) & \text{if } u^*_x(k_c+\ell_c)< 0 \text{ and } \sigma_c(k_c+\ell_c)=1\,. \end{cases}$$

The corresponding switch positions are identified based on the polarity of the modulating signal

$$\sigma_x(u^*_x) = \begin{cases} 1 & \text{if } u^*_x \geq 0 \\ -1 & \text{if } u^*_x < 0 \end{cases}$$

and the sign of the carrier slope σ_c. The (ℓ_c+1)th switch position in phase x follows as

$$u_{x(\ell_c+1)} = \frac{1}{2}\big(\sigma_x(u^*_x(k_c+\ell_c)) - \sigma_c(k_c+\ell_c)\big)\,. \tag{11}$$

D. Pattern Controller

The pattern controller manipulates the switching instants of the switching pattern to achieve fast closed-loop control of the stator flux. One specific example of a pattern controller, deadbeat control, is outlined hereafter.

The controller operates at the sampling instants $t = kT_s$, where $T_s \ll T_c$. The inputs to the controller are the flux error $\boldsymbol{\psi}_{s,\mathrm{err},\alpha\beta}$ and for each phase x, with $x \in \{a,b,c\}$, a switching table with the pair of vectors T^*_x and U_x.

The vector $T^*_x = [t^*_{x1}\ t^*_{x2}\ \ldots t^*_{xn_x}]^T$ captures the nominal switching instants. In carrier-based MP^{3}C, these switching instants are given relative to the carrier sampling instant t_c. At the input to the pattern controller, we redefine the nominal switching instants as $t^*_{xi} = t^*_{xi} - (t - t_c)$. As a result, by subtracting the time interval $t - t_c$, the nominal switching instants in T^*_x are defined relative to the current time instant t, see also Fig. 2. When using OPPs, no modification of T^*_x is required.

The vector U_x contains the single-phase switch positions of phase x. To denote changes in the switch positions, we introduce for phase x the ith switching transition $\Delta u_{xi} = u_{xi} - u_{x(i-1)}$ from the switch position $u_{x(i-1)}$ to u_{xi}. Typically, Δu_{xi} is limited to $\{-1,1\}$, but $\{-2,-1,1,2\}$ etc. is also possible during large transients and disturbances.

The control algorithm is summarized in the following.

Step 1. The required stator flux correction is translated from orthogonal coordinates to abc according to $\Delta\boldsymbol{\psi}_{s,abc} = \tilde{\boldsymbol{K}}^{-1}\boldsymbol{\psi}_{s,\mathrm{err},\alpha\beta}$.

Step 2. The flux correction is scaled by the inverse of the instantaneous dc-link voltage to make it independent thereof. To this end, we introduce $\Delta\boldsymbol{\psi}'_{s,abc} = [\Delta\boldsymbol{\psi}'_{sa}\ \Delta\boldsymbol{\psi}'_{sb}\ \Delta\boldsymbol{\psi}'_{sc}]^T$ and define $\Delta\boldsymbol{\psi}'_{s,abc} = 2/v_{\mathrm{dc}}\,\Delta\boldsymbol{\psi}_{s,abc}$. For phase a, for example, this implies that the required volt-second modification in phase a is achieved by modifying n_a switching transitions by Δt_{ai}, i.e.,

$$\Delta\psi'_{sa} = -\sum_{i=1}^{n_a} \Delta u_{ai}\Delta t_{ai}\,. \tag{12}$$

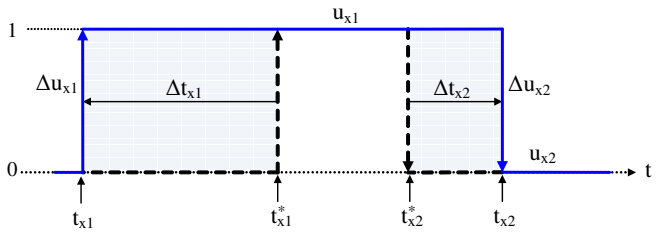

Fig. 5: Example of switching instant modification in phase x with $n_x = 2$ switching transitions

Equivalent statements hold for phases b and c.

Step 3. We consider phase x and set $i = 1$. For the ith switching transition in this phase with the nominal switching instant t^*_{xi} and the switching transition Δu_{xi}, the following operations are performed, see also Fig. 5:

1) The desired modification $\Delta t_{xi} = -\Delta\psi'_{sx}/\Delta u_{xi}$ is computed.
2) The switching instant is modified to $t_{xi} = t^*_{xi} + \Delta t_{xi}$.
3) The switching instant t_{xi} is constrained by imposing timing constraints. For $i = 1$ we impose $0 \leq t_{x1} \leq t^*_{x2}$, whereas for $i > 1$ we impose $t_{x(i-1)} \leq t_{xi} \leq t^*_{x(i+1)}$.
4) The desired volt-second correction in phase x is updated by replacing $\Delta\psi'_{sx}$ with $\Delta\psi'_{sx} + \Delta u_{xi}(t_{xi} - t^*_{xi})$.

While the desired volt-second correction $\Delta\psi'_{sx}$ in this phase is nonzero and a stopping criteria on i (such as $i = n_x$) has not been reached, $i = i + 1$ is set and this procedure is repeated for the next switching transition. Step 3 is performed for each of the three phases.

Even though at time kT_s a sequence of switch positions is planned over a long prediction horizon, only the switching sequence over the sampling interval T_s is applied to the inverter. The predictions are recomputed at the next sampling instant $(k+1)T_s$ using new measurements; a shifted—and if necessary revised—sequence of switch positions is derived. This is referred to as the *receding horizon policy* [13]. This policy provides feedback and makes MP^{3}C robust to flux observer noise and modeling errors.

V. Performance Analysis

Consider an NPC voltage source inverter connected to a medium-voltage induction machine and a constant mechanical

Induction machine	Voltage	3300 V	R_s	0.0108 pu
	Current	356 A	R_r	0.0091 pu
	Real power	1.587 MW	X_{ls}	0.1493 pu
	Apparent power	2.035 MVA	X_{lr}	0.1104 pu
	Frequency	50 Hz	X_m	2.3489 pu
	Rotational speed	596 rpm		
Inverter			v_{dc}	1.930 pu
			X_c	5.380 pu

TABLE II: Rated values (left) and parameters (right) of the drive

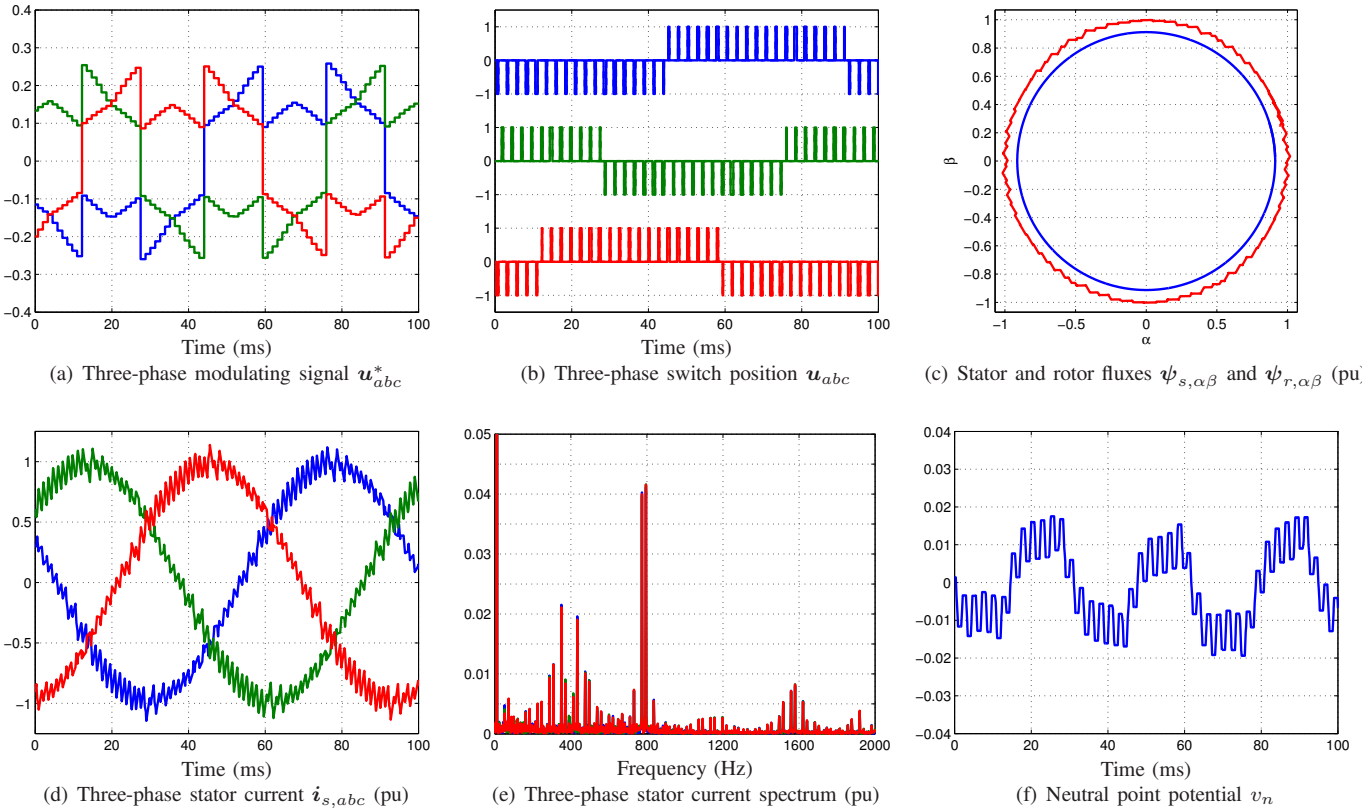

(a) Three-phase modulating signal $\boldsymbol{u}^*_{abc}$ (b) Three-phase switch position $\boldsymbol{u}_{abc}$ (c) Stator and rotor fluxes $\boldsymbol{\psi}_{s,\alpha\beta}$ and $\boldsymbol{\psi}_{r,\alpha\beta}$ (pu)

(d) Three-phase stator current $\boldsymbol{i}_{s,abc}$ (pu) (e) Three-phase stator current spectrum (pu) (f) Neutral point potential v_n

Fig. 6: Carrier-based MP^{3}C operating at the fundamental frequency $f_1 = 10\,\text{Hz}$ and rated torque. The carrier frequency is $f_c = 200\,\text{Hz}$

load. A 3.3 kV and 50 Hz squirrel-cage induction machine rated at 2 MVA with a total leakage inductance of 0.25 per unit (pu) is used as an example of a typical medium-voltage induction machine. The total dc-link voltage is $v_{\text{dc}} = 5.2\,\text{kV}$. The detailed parameters of the machine and inverter are summarized in Table II.

The per unit (pu) system is established using the base quantities $V_B = \sqrt{2/3}V_{\text{rat}} = 2694\,\text{V}$, $I_B = \sqrt{2}I_{\text{rat}} = 503.5\,\text{A}$ and $f_B = f_{\text{rat}} = 50\,\text{Hz}$, with V_{rat}, I_{rat} and f_{rat} referring to the rated voltage, current and frequency, respectively.

A. Normal-Speed Operation

Consider operation with carrier-based MP^{3}C and the carrier frequency $f_c = 400\,\text{Hz}$. This leads to a device switching frequency of approximately 200 Hz. Fig. 6 shows simulation results over 100 ms. The drive is operated at rated torque and 20% speed with the fundamental frequency $f_1 = 10\,\text{Hz}$. The corresponding pulse number is $d = 20$. The modulating signal is shown in Fig. 6(a), to which a min/max common-mode component was added to produce switching patterns that are equivalent to SVM. The resulting three-phase switch positions are shown in Fig. 6(b).

Fig. 6(c) shows the (piecewise affine) trajectory of the stator flux vector in the stationary orthogonal $\alpha\beta$ coordinate system. The stator flux trajectory is almost circular at this high pulse number. The rotor flux trajectory is the inner circular trajectory. The three-phase stator currents of the machine are shown in Fig. 6(d). The corresponding harmonic amplitude spectrum of the stator current, see Fig. 6(e), was computed over five fundamental periods. The total demand distortion (TDD) of the stator current is 7.5%. The NP potential is shown in Fig. 6(f). The strong periodic fluctuations are caused by the SVM-type common-mode voltage injection, see also Fig. 6(a).

B. Low-Speed Operation

Operation at very low speed is exemplified in Fig. 7, where the drive is operated at the fundamental frequency $f_1 = 1.5\,\text{Hz}$ and rated torque. Simulations results over 100 ms are shown. The carrier frequency is kept at $f_c = 400\,\text{Hz}$, resulting in the high pulse number $d = 200$. The modulating signal is close to zero. A common-mode offset of the amplitude $\hat{u}_0 = 0.1$ is added to the three-phase modulating signal, see Fig. 7(a). The large offset $\pm\hat{u}_0$ shifts the three-phase modulating signal completely into the upper or the lower half and ensures a switching pattern with non-zero pulse width, see Fig. 7(b).

Whenever the NP potential hits its bounds at ± 0.025, the hysteresis controller (6) flips the sign of the common-mode component. This happens at the time instants $t = 17.5\,\text{ms}$, $52.5\,\text{ms}$ and $85\,\text{ms}$. Despite the significant common-mode component, the stator currents are almost sinusoidal, as can seen in Fig. 7(d). The harmonic current spectrum in Fig. 7(e) resembles that of sinusoidal CB-PWM with sidebands around

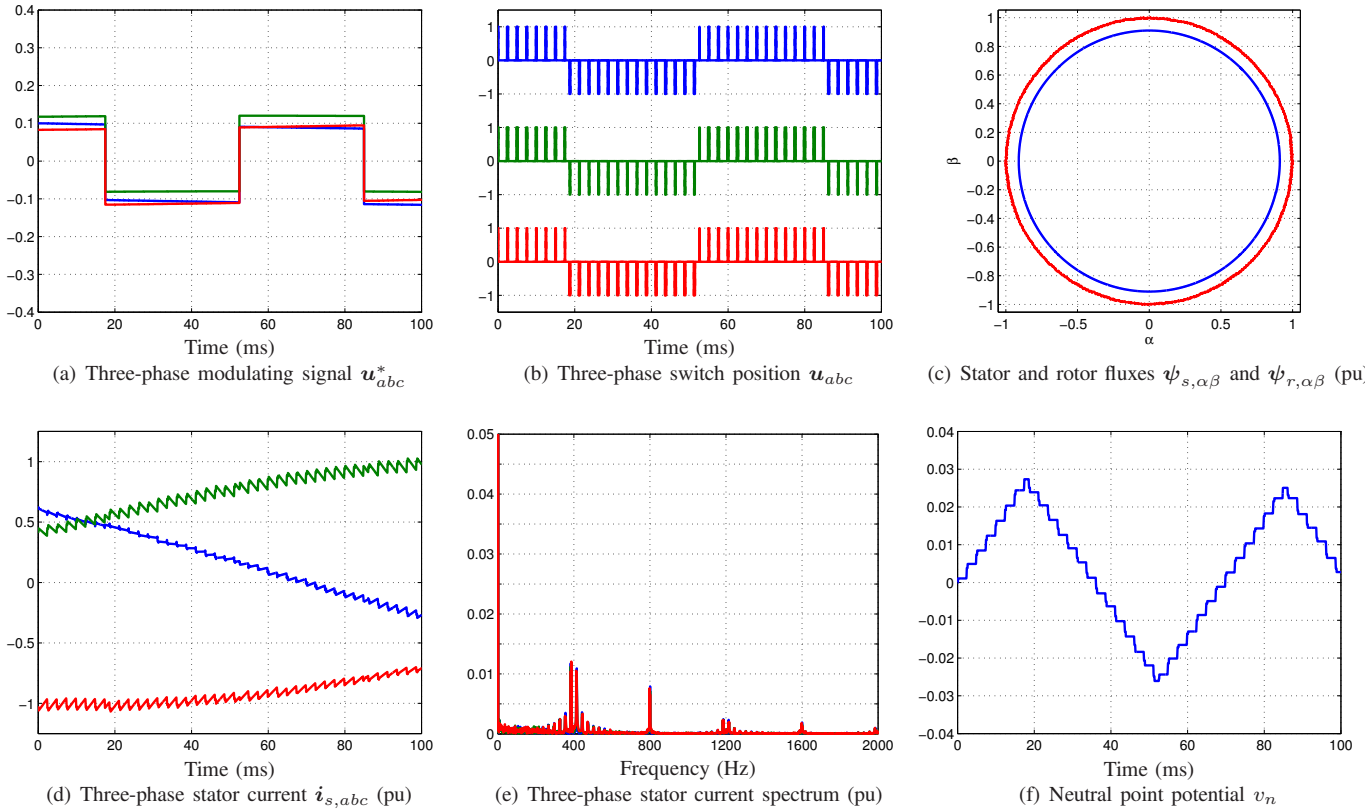

(a) Three-phase modulating signal $\boldsymbol{u}^*_{abc}$ (b) Three-phase switch position $\boldsymbol{u}_{abc}$ (c) Stator and rotor fluxes $\boldsymbol{\psi}_{s,\alpha\beta}$ and $\boldsymbol{\psi}_{r,\alpha\beta}$ (pu)

(d) Three-phase stator current $\boldsymbol{i}_{s,abc}$ (pu) (e) Three-phase stator current spectrum (pu) (f) Neutral point potential v_n

Fig. 7: Carrier-based MP^{3}C operating at the fundamental frequency $f_1 = 1.5\,\text{Hz}$ and rated torque. The carrier frequency is $f_c = 200\,\text{Hz}$. The NP potential is controlled by modifying the sign of the injected common-mode component

integer multiples of the carrier frequency $f_c = 400\,\text{Hz}$. The stator current TDD is 3.0%.

The common-mode component (7) could be added to the three-phase modulating signal to achieve a SVM switching pattern. This implies that two common-mode components could be used when operating at very low speeds; one component is added to achieve SVM-type switching and the second one, $\pm\hat{u}_0$, ensures a minimum pulse width. The benefit of this approach are reduced current distortions.

C. Transition Between OPPs and Online Generated Switching Patterns

The switch from OPP-based to carrier-based MP^{3}C at time instant $t = 0\,\text{ms}$ is depicted in Fig. 8 when operating at close to rated speed. Before $t = 0$, an OPP with pulse number $d = 11$ was used in the standard MP^{3}C setup, whereas after time $t = 0$, the switching patterns are generated online with the carrier to fundamental frequency ratio $f_c/f_1 = 22$. The switching frequency thus remains approximately constant.

Fig. 8(a) confirms that the change in switching patterns does not cause any transient or disturbance. At time $t = 0$, the shape of the flux reference changes from piecewise affine (for OPPs) to sinusoidal (for carrier-based MP^{3}C). The stator flux ripple increases with the online generated switching patterns, since these switching patterns and their flux trajectory are suboptimal with respect to an OPP.

The corresponding three-phase switch positions are depicted in Fig. 8(b). The transition from OPPs to CB-PWM switching patterns with a fixed modulation cycle at time $t = 0$ is clearly visible.

VI. Conclusions

As shown, MP^{3}C can be extended to all speed operating points of a variable speed drive. At high fundamental frequencies, offline-computed OPPs serve as switching patterns. At low fundamental frequencies, the three-phase stator voltage reference can be computed. Using the principle of CB-PWM, this reference voltage is translated into a suitable three-phase switching pattern. This online-generated switching pattern extends over multiple modulation cycles, covering the prediction horizon of MP^{3}C. The CB-PWM switching pattern is not directly applied to the converter; instead, it is fed to the MP^{3}C pattern controller, which modifies the switching instants of the switching pattern, thus controling the stator flux vector along its reference trajectory.

Switching between different control methods and re-initialization of the integrator states of the corresponding controller is thus avoided. By inserting pulses during torque steps, MP^{3}C achieves as short torque transients as direct torque control [9], regardless of whether OPPs or CB-PWM generated switching patterns are used.

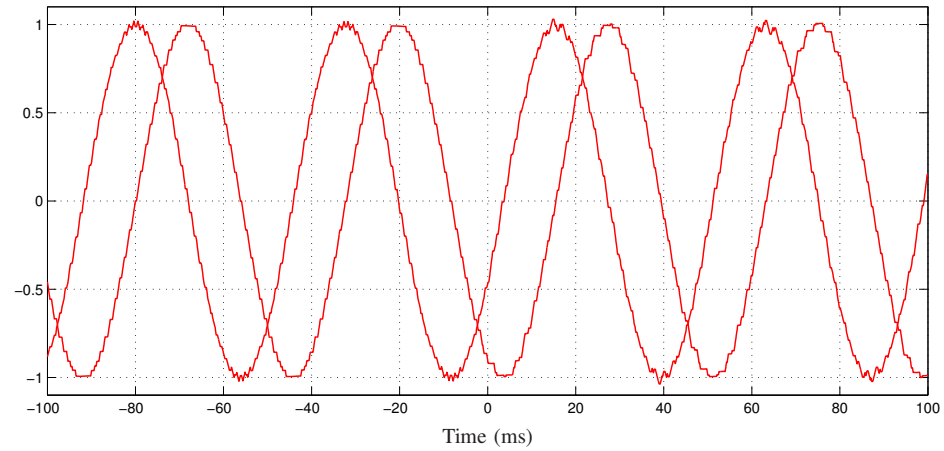

(a) Stator flux $\boldsymbol{\psi}_{s,\alpha\beta}$ with its α- and β-components

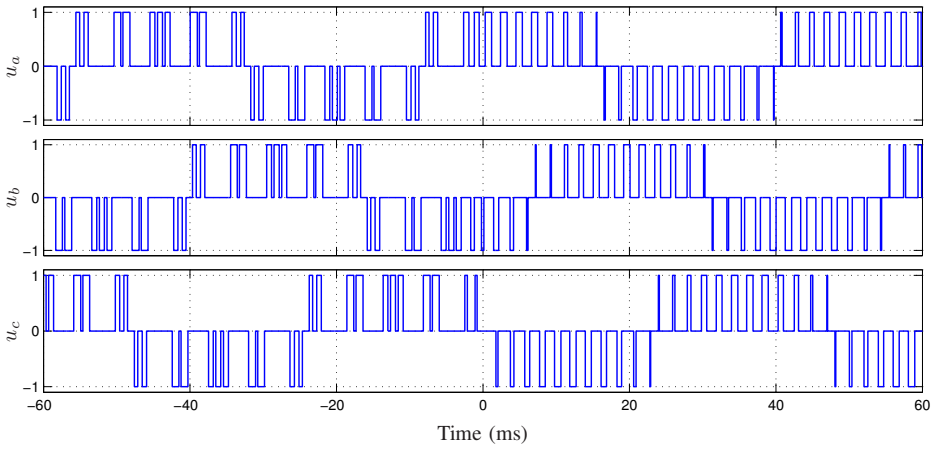

(b) Three-phase switch position $\boldsymbol{u}_{abc}$

Fig. 8: Transition from OPP-based MP^{3}C (left) to carrier-based MP^{3}C (right) at time instant $t = 0\,\text{ms}$

ACKNOWLEDGMENT

The authors appreciate the help of Andrea Rüetschi in implementing and refining the carrier-based MP^{3}C concept.

REFERENCES

[1] H. S. Patel and R. G. Hoft, "Generalized techniques of harmonic elimination and voltage control in thyristor inverters: Part I–Harmonic elimination," *IEEE Trans. Ind. Appl.*, vol. IA-9, pp. 310–317, May/Jun. 1973.

[2] D. G. Holmes and T. A. Lipo, *Pulse width modulation for power converters: Principles and practice*. IEEE Press, 2003.

[3] G. S. Buja, "Optimum output waveforms in PWM inverters," *IEEE Trans. Ind. Appl.*, vol. 16, pp. 830–836, Nov./Dec. 1980.

[4] T. Geyer, *Model predictive control of high power converters and industrial drives*. London, UK: Wiley, Oct. 2016.

[5] J. Holtz and N. Oikonomou, "Fast dynamic control of medium voltage drives operating at very low switching frequency—An overview," *IEEE Trans. Ind. Electron.*, vol. 55, pp. 1005–1013, Mar. 2008.

[6] N. Oikonomou, C. Gutscher, P. Karamanakos, F. Kieferndorf, and T. Geyer, "Model predictive pulse pattern control for the five-level active neutral-point-clamped inverter," *IEEE Trans. Ind. Appl.*, vol. 49, pp. 2583–2592, Dec. 2013.

[7] T. Geyer, N. Oikonomou, G. Papafotiou, and F. Kieferndorf, "Model predictive pulse pattern control," *IEEE Trans. Ind. Appl.*, vol. 48, pp. 663–676, Mar./Apr. 2012.

[8] V. Spudic, E. Rohr, T. Geyer, and P. Al Hokayem, "Controlling a three-phase electrical converter," 2015. EP 15 177 656 A1.

[9] T. Geyer and N. Oikonomou, "Model predictive pulse pattern control with very fast transient responses," in *Proc. IEEE Energy Convers. Congr. Expo.*, (Pittsburgh, PA, USA), Sep. 2014.

[10] B. P. McGrath, D. G. Holmes, and T. Lipo, "Optimized space vector switching sequences for multilevel inverters," *IEEE Trans. Power Electron.*, vol. 18, pp. 1293–1301, Nov. 2003.

[11] S. Ogasawara and H. Akagi, "Analysis of variation of neutral point potential in neutral-point-clamped voltage source PWM inverters," in *Proc. IEEE Ind. Appl. Soc. Annu. Mtg.*, Oct. 1993.

[12] J. K. Steinke, "Switching frequency optimal PWM control of a three-level inverter," *IEEE Trans. Power Electron.*, vol. 7, pp. 487–496, Jul. 1992.

[13] J. B. Rawlings and D. Q. Mayne, *Model predictive control: Theory and design*. Madison, WI, USA: Nob Hill Publ., 2009.